Article

Effect of High-Temperature Annealing on Raman Characteristics of Silicon Nanowire Arrays

Shanshan Wang [1,*] and Yan Zhang [2]

1 School of Electronic Information Engineering, Xi'an Technological University, Xi'an 710021, China
2 School of Optoelectronic Engineering, Xi'an Technological University, Xi'an 710021, China
* Correspondence: wangshanshan@xatu.edu.cn

Abstract: We demonstrate two distinct experimental processes involving the large-area growth of ordered and disordered silicon nanowire arrays (SiNWs) on a p-type silicon substrate using the metal-assisted chemical etching method. The two processes are based on the etching of monocrystalline silicon wafers by randomly distributed Ag films and ultra-thin Au films with ordered nano-mesh arrays, respectively, wherein the growth of SiNWs is implemented using a specific proportion of a HF-containing solution at room temperature. In this study, the microstructural change mechanisms for the two morphologically different arrays before and after annealing were investigated using Raman spectra. The effects of various mechanisms on the observed Raman scattering peak's deviation from symmetry, redshift and broadening were analyzed. The evolution of the unstable amorphous structures of nanoscale materials during the high-temperature annealing process was observed via high-resolution scanning electron microscope (SEM) observations. The scattering peak parameters determined from the Raman spectra led to conclusions concerning the various mechanisms by which high-temperature annealing influences the microstructures of the two morphologically different SiNWs fabricated on the p-type silicon substrate. Therefore, the deviation of SiNWs from the monocrystalline silicon scattering peak at 520.05 cm^{-1} when changing the diameter of the nanowire columns was calculated to further analyze the effect of thermal annealing on Raman characteristics.

Keywords: silicon nanowire arrays; microstructural change mechanism; Raman spectra; high-temperature annealing; the magnitude of redshift

1. Introduction

Innovative photoelectric detection applications of low-dimensional nanomaterials have attracted extensive attention due to their ability to lower power consumption and extend the lifetime of detection equipment and due to their light-trapping effect, making them suitable for anti-reflection coatings [1–3]. Silicon nanowire arrays, as promising materials, provide special large-area surface textures for strongly increasing the absorption of incident light in the visible to infrared region and have been successfully exploited as high-performance photodetectors to rapidly and accurately detect light waves that exist in the current environment. Therefore, SiNWs exhibit scalable applications with large industrial infrastructures for low-cost and high-yield processing in various technological fields, such as biosensors, self-powered ultraviolet photodetectors, photovoltaic devices and lithium-ion batteries [4–8]. In recent years, various methods have been reported for synthetizing one-dimensional nanomaterials. Electrochemical synthesis using inorganic molten salts as electrolytes has achieved great success in assembling nanomaterials, as well as the extraction of other active metals. Simon Schweidler et al. [9] studied the degradation behavior of a high-entropy oxyfluoride cathode material in lithium cells during electrochemical cycling in situ via acoustic emission monitoring. Yifan Dong et al. [10] developed a more sustainable method to produce silicon nanowires in bulk quantities through the direct electrochemical reduction of $CaSiO_3$. Takashi Okazoe et al. [11] reported

the synthesis of a perfluoropolyether derivative that possesses –(CF_2CF_2O)– as a repeating unit. However, the synthesis process of materials can be affected by many external experimental factors, such as process conditions, as well as the ionic concentration of the electrolyte. Last year, Gao Sen et al. [12] prepared highly dense and vertically aligned sub-5 nm silicon nanowires with length/diameter aspect ratios greater than 10,000 by developing a catalyst-free chemical vapor etching process and successfully observed an unusual lattice reduction of up to 20% within ultra-narrow silicon nanowires.

Metal-assisted chemical etching (MACE) is advantageous compared with conventional methodologies such as chemical vapor deposition (CVD), Thermal Evaporation (TE), laser ablation, electrochemical synthesis and electron beam lithography because of its moderate reaction conditions, convenient operation and short fabrication period for the synthetic process [13–15]. The noble metal constituting a dense layer deposited on monocrystalline silicon as an etching catalyst used in MACE is a key factor in the anisotropic etching process. In this work, randomly distributed Ag films and ultra-thin Au films with ordered nanomesh arrays of appropriate thickness were deposited via chemical reaction and ion sputtering, respectively. Noble metal particles in a HF-containing solution tend to form ordered and disordered porous structures due to metal-induced localized etching of the surface of a silicon wafer [16,17]. Owing to the addition of organic or inorganic chemical reagents to the experimental process, the catalysis of noble metals and stress generated during etching, there is inevitable damage to the integrity of the crystal lattice and the formation of contaminated membrane layers, thus inducing lattice distortion and changing the simple harmonic vibration of the lattice. Structural defects, surface impurities and non-dense sensitive elements for SiNWs strongly influence the physical properties of materials, further affecting the external photoelectric effect. Above all, the quantum confinement effect caused by etching bulk silicon into nanowires induced modified physical properties, as revealed by the presence of a frequency shift, broadening and asymmetry in the corresponding Raman spectra [18]. In this article, the effects of various mechanisms on the observed Raman scattering peak's deviation from symmetry, redshift and broadening are analyzed. Therefore, we investigated the deviation of SiNWs from the monocrystalline silicon scattering peak by changing the diameter of the nanowire columns through thermal expansion to further analyze the effect of high-temperature annealing on Raman characteristics. Raman spectra also serve as a tool for detecting elementary excitations, such as phonon and electron behavior, in semiconductors. The information provided by Raman spectra can assist in improving the external physical effects of solid materials. Moreover, the deeper probing of the morphological characteristics of SiNWs is particularly important not only to improve the sensitivity to incident light and extend the detection band of nanomaterials but also to explore the potential applications of photovoltaic devices and photoelectric sensors with silicon microelectronics so that they may become reality.

2. Experiments

2.1. Pretreatment of Si Wafers

P-type monocrystalline silicon is more suitable for nanowire growth because of the number of holes in the material [19,20] (Zhejiang Lijing Optoelectronic Technology Co., Ltd., Quzhou, China). The parameters of the substrate material are as follows: single polished p-type silicon wafers with 500 ± 10 μm thickness, 100 ± 0.4 mm diameter, <100> crystal orientation and 1–10 Ω·cm resistivity. The cut silicon wafers were cleaned with ethanol (Sinopharm Chemical Reagent Co., Ltd., Shanghai, China), 5%HF (Sinopharm Chemical Reagent Co., Ltd., Shanghai, China) and ammonia solution (Sinopharm Chemical Reagent Co., Ltd., Shanghai, China) in sequence, ultrasonically vibrated for 5 min and dried by high-purity nitrogen at each step to remove the contaminated layers on the surfaces of silicon wafers to the greatest extent possible.

2.2. Deposition of Noble Metal Films

Noble metal films are used in the etching process not only as catalysts but also as spatially restricted templates for nanowire growth [19]. Due to the difference in surface morphology between disordered arrays and ordered arrays, the synthetic methods of noble metal films are also different. One approach is to form a layer of silver film on the surface of a polished silicon wafer by putting pretreated silicon wafers into $AgNO_3$ + HF (Sinopharm Chemical Reagent Co., Ltd., Shanghai, China) mixed solution [21,22]. Previous experiments [17,19,22,23] have demonstrated that the morphologies of SiNWs can be fabricated from monocrystalline silicon with a given orientation by changing the silver-plating time, the proportion of etching solution and the etching time. First, of the whole system, the redox process only takes place at the region of Ag membrane coverage, and the location of Ag particles determines the positioning of silicon wafers subjected to chemical corrosion. Second, the Nernst equation has shown that as the proportion of H_2O_2 in the etching solution increases, the potential energy difference of the battery reaction continues to increase, so the reaction rate also accelerates. Finally, the etching time is too long to damage the integrity of the array, according to an average silicon wire growth rate of about 5.7125 nm/s. The other approach is to form a versatile homogeneous Au film on the surface of a polished silicon wafer by ion sputtering anodic aluminum oxide (AAO) (Topmembranes Technology Co., Ltd., Shenzhen, China) membranes with suitable sputtering parameter settings. The Au film formed in the experiment cannot be broken due to the surface tension of the NaOH solution, nor can the Au nanomesh be blocked by Au particles due to the closure effect [19]. The uniformly distributed Ag films and ordered mesh-patterned Au films on the silicon substrates were characterized using a scanning electron microscope (SEM, SU1510, Hitachi, Tokyo, Japan), as shown in Figure 1.
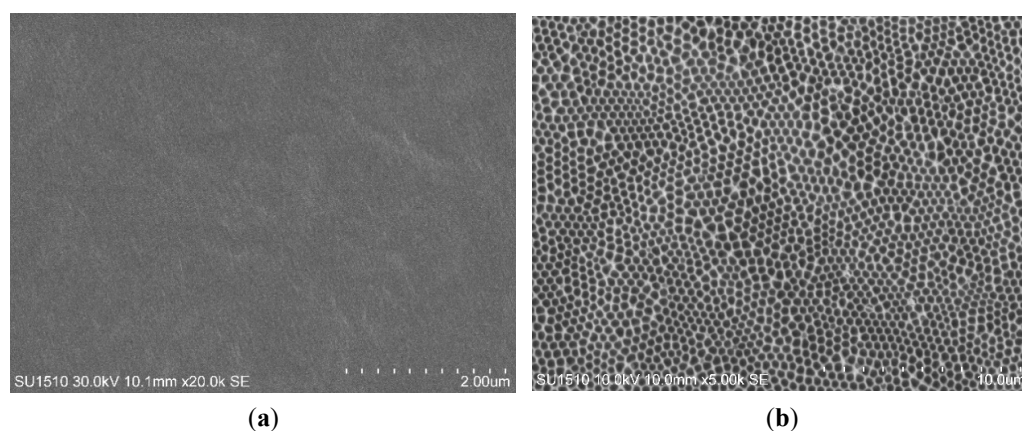

(**a**)   (**b**)

Figure 1. SEM images of noble metal films attached to pretreated silicon wafers: (**a**) Ag nanoparticles formed on the surface of the silicon substrate (HF + $AgNO_3$ = 4.8 mol/L + 0.005 mol/L; silver-plating time: 120 s) [22]; (**b**) ordered nanomesh-patterned Au films formed on the surface of the silicon substrate (sputtering current: 3 mA; sputtering time: 110 s; the number of sputtering applications: two; thickness of Au film: 14.55 nm) [17].

2.3. Metal-Assisted Chemical Etching

The silicon substrates covered with the randomly distributed Ag film and the spatially ordered mesh Au film were placed into the etching solution with a ratio of H_2O_2: HF: H_2O = 5:12:37 for 40 and 50 min, respectively. The microstructures of the two different morphologies were investigated via high-resolution SEM, as shown in Figures 2 and 3.
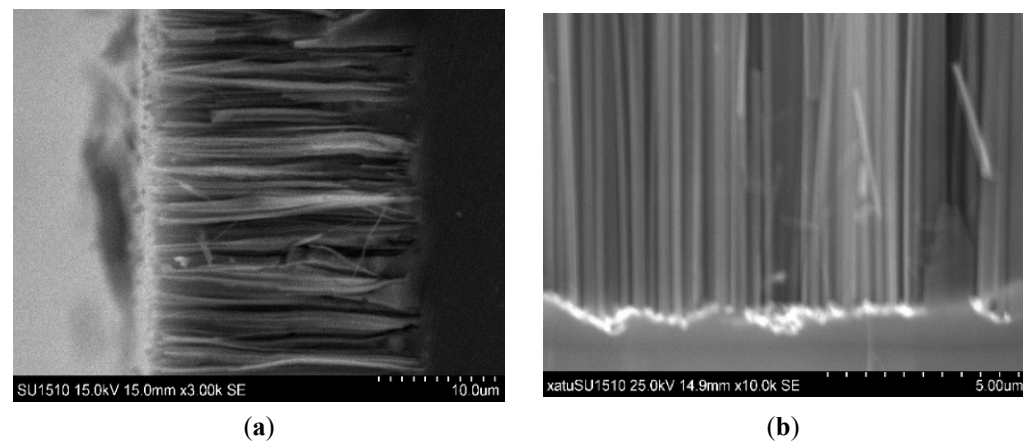
Figure 2. Comparison of cross-sectional views of SiNWs fabricated by two methods: (**a**) SiNWs fabricated with the randomly distributed Ag film; (**b**) SiNWs fabricated with the spatially ordered mesh Au film.

Figure 3. Comparison of top views of SiNWs fabricated by two methods: (**a**) SiNWs fabricated with the randomly distributed Ag film; (**b**) SiNWs fabricated with the spatially ordered mesh Au film.
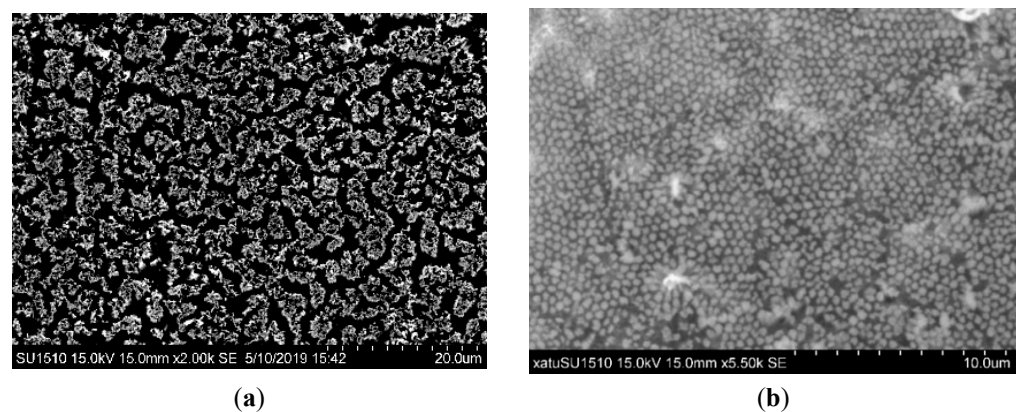
The etching results demonstrate that the morphologies of the grown SiNWs are subject to the pattern of the noble metal film deposited on the silicon substrate surface. The substrate coated with the noble metal film is oxidized to SiO_2 by H_2O_2, which reacts with HF to form water-soluble silicates [15]. In Figures 2a and 3a, randomly distributed Ag nanoparticles gradually sink during the etching process, forming an etching channel perpendicular to the silicon substrate. Eventually, countless disordered tiny columns appear on the entire silicon wafer surface. In Figures 2b and 3b, Au films with regular hexagonal mesh arrays replicated by AAO restrict the growth of silicon wires, fabricating ordered arrays with the precise control of the location, diameter and density on the silicon wafer surface. The synthesis of ordered arrays is evidence of substantial progress in the controlled preparation of SiNWs.

2.4. Annealing Process

Annealing technology is widely applied in the advanced optical sensing field to improve the photoelectric properties of microstructured materials. James E. Carey et al. [24] prepared microstructured silicon and measured the spectral responsivity between 400 and 1600 nm at room temperature. They found that the samples were annealed at 825 K for 30 min, which preserved the high concentration of interior atoms in unique nonequilibrium conditions, leading to high gain and photoresponse in the visible to near-infrared region. For reference, the two differently treated samples were annealed for 30 min at the thermodynamic temperature of 825 K in a Lindberg/blue M tubular furnace (TF55035KC-1, Thermo Fisher Scientific, Waltham, MA, USA). The samples placed in the quartz tank were first

pushed into the plexiglass tube of a tubular furnace. Argon gas of 200 sccm was pumped to isolate the samples from the air. Then, argon gas of 100 sccm was pumped continuously at a constant temperature. The microstructures of the samples were observed by SEM in Figure 4.
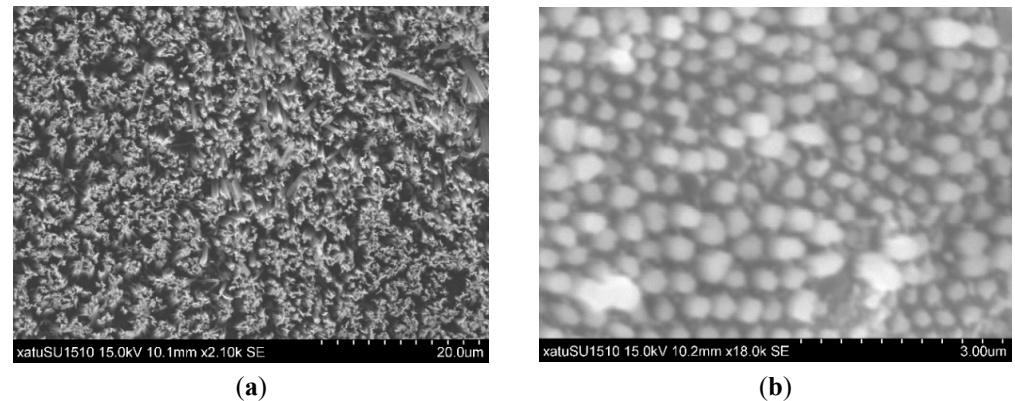

(**a**)

(**b**)

Figure 4. Microstructural images of two differently treated samples after annealing: (**a**) SiNWs fabricated with the randomly distributed Ag film; (**b**) SiNWs fabricated with the spatially ordered mesh Au film.

3. Raman Spectroscopy Test

Since SiNWs are expected to be used as advanced materials to detect light waves for achieving efficient photoelectric conversion, it is necessary to further investigate the internal structural characteristics of samples and clarify the influence of high-temperature annealing on material properties. The Raman scattering spectra of the samples were recorded by using a HORIBA XploRA PLUS intelligent fully automatic Raman spectrometer with a 532 nm wavelength optically excited laser (XploRA PLUS, HORIBA Jobin Yvon, Paris, France). It is a high-performance and sophisticated Raman spectrometer with a micro confocal function that can provide the fastest data acquisition speed of 1600 spectral lines/s and an imaging speed of more than 1 ms/pixel. Figure 5 shows the Raman spectra for samples fabricated by two distinct experimental processes before and after annealing.
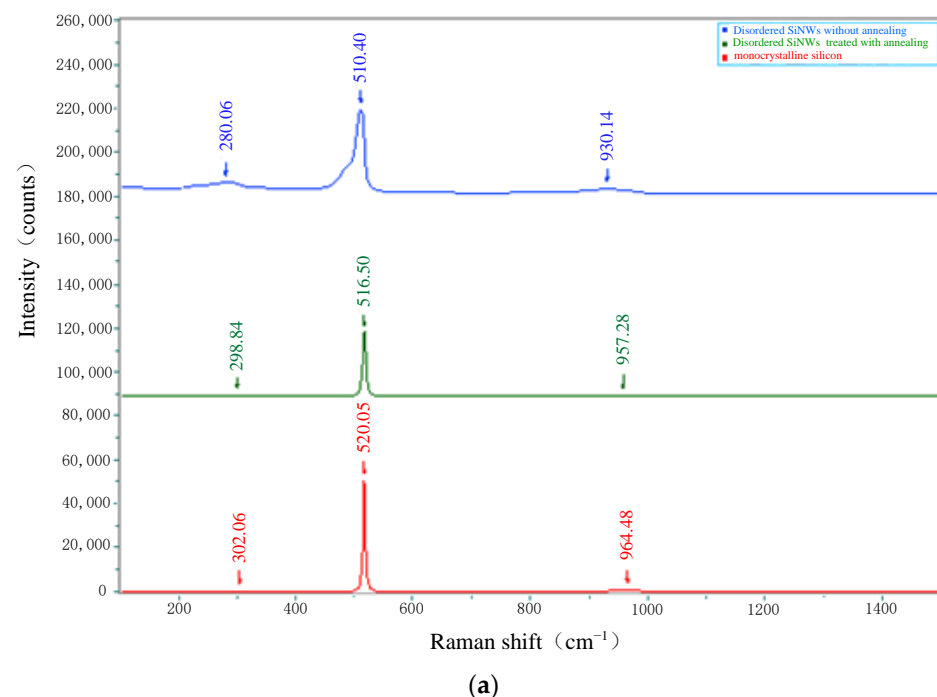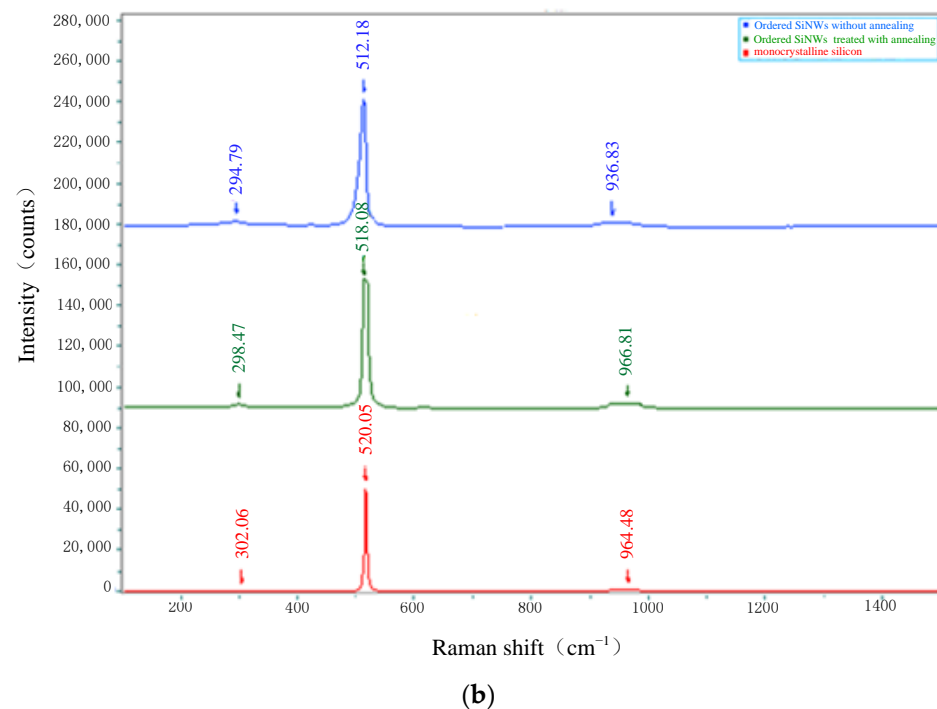

(**a**)

Figure 5. *Cont.*

(b)

Figure 5. The comparison of Raman spectral curves of SiNWs fabricated by two methods: (**a**) SiNWs fabricated with randomly distributed Ag film; (**b**) SiNWs fabricated with the spatially ordered mesh Au film.

4. Discussion

Figures 3 and 4 show the microstructural comparison of SiNWs before and after annealing. Before annealing, the surface of the SiNWs fabricated with randomly distributed Ag films presents a dendritic microstructure with high porosity, and the surface of the substrate coated with the spatially ordered mesh Au films form numerous tiny nanowire columns whose structures are consistent with the morphology of the Au nanomesh. After annealing, both of the surficial structures of the two morphologically different arrays are thermally expanded. The nanowires of disordered arrays are clustered, causing an increase in the interfacial area. Meanwhile, the adjacent wire spacing of the ordered arrays becomes denser, presenting a more uniform distribution in the volume of the etching layer.

Due to the internal carrier transport mechanism and external experimental conditions, it is inevitable that intrinsic and extrinsic lattice defects destroy the crystal symmetry in the constituting areas, and stress produced by noble metal catalysts in the etching process changes the phonon vibration frequency. We found that a large number of bubbles generated during the chemical etching process produce huge stress on the surfaces of silicon columns, which causes defects and microcracks in the relatively fragile grain boundaries. Simultaneously, calculations showed that more vacancies exist on the grain boundary in the disordered array than in the ordered array, and they are generated in the process of nanowires being pressed from blocks into particles. The first experiment revealed that the high surface activity of the Ag film produces excess positive holes, which diffuse to the top or side wall of silicon wires [17], resulting in secondary etching for disordered arrays. However, the interaction of HF with AgNO$_3$ during the silver-plating process can lead to the formation of nitric acid, which, together with HF, will etch silicon. When etching monocrystalline Si wafers, vacancies are formed that will merge into the pores. Naturally, places that are covered with metal will not be as etched as places free of coating. During the preparation of the ordered array, the AAO membranes need to be removed as sacrificial layers. It is quite possible that there is an associated increase in the unintentional deposition of residual aluminum oxide on arrays due to the NaOH solution not completely dissolving AAO, which would affect the probability of carrier recombination.

Higher activation energy generated by the initial high-temperature annealing is provided to the deviated silicon atoms. This makes it possible to promote the diffusion of oxygen atoms into the material, accelerating oxidation. The oxide formation process mainly includes the combination of O-containing bonds and suspended bonds after H removal from the surface of nanowires. The small amount of oxide and grains with different shapes appearing on the surface of the array could be observed after annealing. It is conjectured that there exists an amorphous and polycrystalline layer containing many silicon nanoclusters embedded in oxidized silicon on the surface [25]. During the high-temperature heating process, the adsorbed silicon atoms and silica particles receive enough energy to diffuse into the amorphous and polycrystalline layers. Moreover, pores existing on the top and side of silicon nanowires could contract when heat is applied, or even disappear, indicating the formation of compact films. It should be noted that the structural evolution of SiNWs is dependent on the annealing time and temperature. The homogeneity of the microstructured arrays can be obtained by setting moderate annealing conditions.

SiNWs samples with different structures before and after annealing used for the Raman scattering study were synthesized using various types of noble metal film catalysts with different morphologies. As shown in Figure 5, we can see the related assignment of scattering peaks in the Raman spectra of prepared samples. The main strong sharp peak of monocrystalline silicon is measured at 520.05 cm^{-1} with a symmetric lineshape, which derives from first-order optical phonon scattering with triple-degenerate Γ 25. In addition to the main peak with the highest intensity, there are two broad peaks with very weak intensity at 302.06 cm^{-1} and 964.48 cm^{-1}, which are transverse optical biphonon peak (2TO) and transverse acoustic biphonon peak (2TA) scattering, respectively. The biphonon peak is caused by two consecutive single-phonon Raman scattering events, so the frequency shift of the biphonon spectrum should be the sum or difference of the single-phonon spectrum frequency shift [26]. The scattering intensities measured in Raman spectra can lead to conclusions concerning microstructural parameters such as bonding, as well as deviations from the ideal crystalline structure [27].

The characteristic values of the measured Raman bands can vary significantly depending upon which peak profile function is used in the fitting [28]. After the comparison of the main peak fitting profile by Gaussian, Lorentzian and Gaussian–Lorentzian functional forms in LabSpec 6.3 software, the Gaussian fitting profile was used for the Raman spectra analysis of four test samples to realize the peak-splitting fitting calculation of superimposed peaks and obtain corresponding characteristic parameters, including the peak position, peak intensity, half-height width and peak area. The original spectral information is characterized by the feature parameters obtained from Gaussian peak fitting, and the fitting results are shown in Figures 6 and 7.
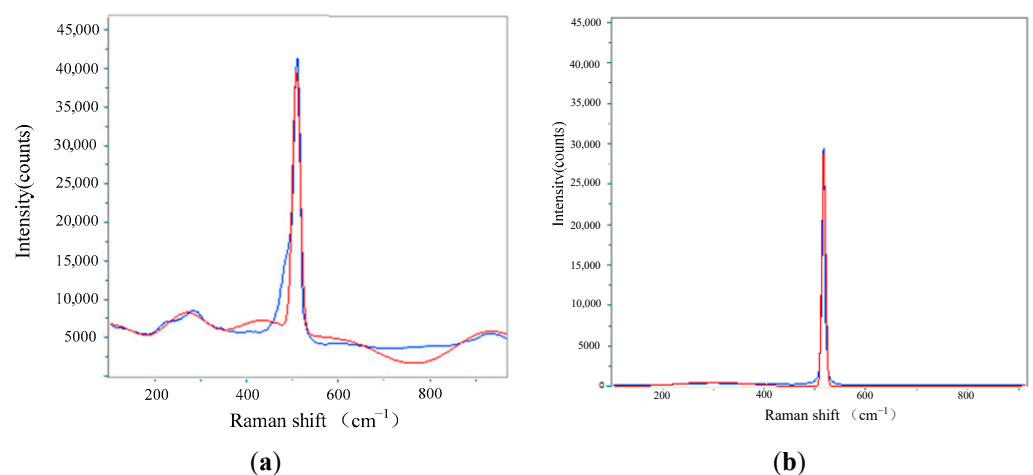

Figure 6. Gaussian peak fitting diagram of Raman spectra of disordered SiNWs. (**a**) Before annealing. (**b**) After annealing.
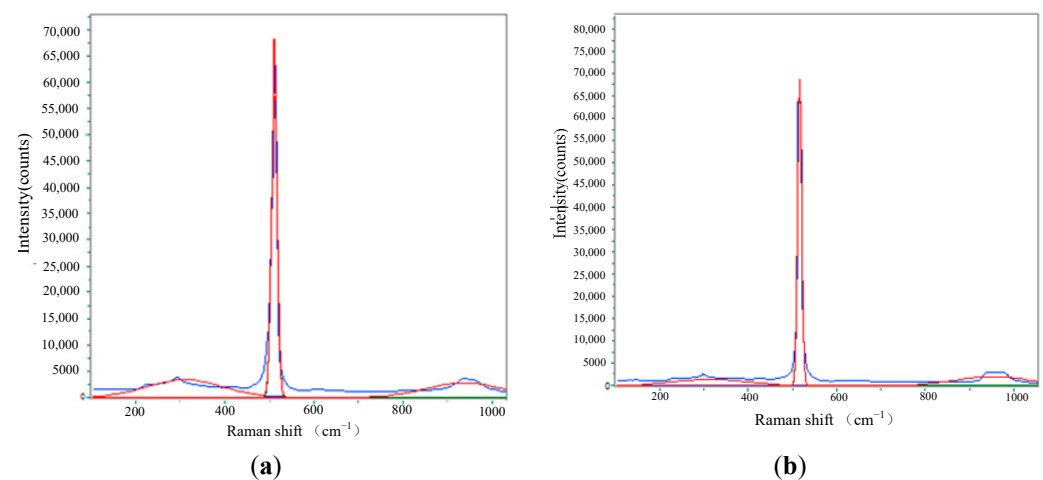
Figure 7. Gaussian peak fitting diagram of Raman spectra of and ordered SiNWs. (**a**) Before annealing. (**b**) After annealing.

In Figure 5, the main peaks around 510.04 cm^{-1} (disordered SiNWs without annealing), 516.5 cm^{-1} (disordered SiNWs with annealing), 512.18 cm^{-1} (ordered SiNWs without annealing) and 518.08 cm^{-1} (ordered SiNWs with annealing) move toward lower frequencies. Because of first-order optical phonon scattering, the representative Raman peak of monocrystalline silicon appears at 520 cm^{-1}. As shown in Figure 4b, the diameter of the annealed nanowire columns is 0.3 μm; this value is then substituted into the following formula [29,30]:

$$d = 2\pi \left(\frac{B}{\omega_{\mathrm{b}} - \omega_{\mathrm{n}}} \right)^{0.5} \tag{1}$$

where d is the diameter of the nanowire columns, B is a constant related to the material, ω_{b} is the crystalline TO peak location of monocrystalline silicon, and ω_{n} is the TO peak location for SiNWs. $\omega_{\mathrm{b}} - \omega_{\mathrm{n}}$ is the deviation of the measured SiNWs peak location from the monocrystalline silicon peak at 520.05 cm^{-1}. We can deduce $B = 4496$ cm^{-1} nm^2 from the integrated Raman scattering peak intensity at 520.05 cm^{-1} and at around 518.08 cm^{-1} with ordered SiNWs after annealing. We also calculated the estimated value of the diameter of disordered nanowire columns before and after annealing to be 135.553 nm and 223.49 nm, respectively. According to the calculation results, the relationship curve between $\omega_{\mathrm{b}} - \omega_{\mathrm{n}}$ and the nanowire columns d is plotted.

As shown in Figure 8, the deviation of two samples with thermal expansion from the monocrystalline silicon peak at 520.05 cm^{-1} is smaller compared with arrays without annealing. This can be attributed to the progressive decrease in the lattice constant as a function of the nanowire column size, which has an impact on the phonon vibration frequency. The problem associated with the redshift of scattering peaks becomes worse as the phonon vibration frequency increases. According to measurements of ordered arrays, the redshift characteristics arise as the diameter of the nanowire columns increases. For each 150 nm increase in diameter, the deviation decreases by approximately 5.9 cm^{-1}.

A preliminary test revealed that the redshift and broadening of the main peak of the ordered array are weaker than those of the disordered array. Besides the existence of an amorphous and polycrystalline layer caused by extremely tiny nanowires in the disordered array, this would have been affected by the morphology and type of the noble metal catalyst causing ambient pressure in the synthesis process of silicon wires. The interface between the silicon nanowires and the substrate generates external stress induced by the space constraints of noble metal films, as well as the residual stress caused by the capillary effect of liquid volatilization. The existence of external stress changes the bond length between internal molecules, thus changing the vibration frequency of the lattice and causing a change in the spectral lineshape. During the etching process, the external stress produced by the catalytic etching of the Ag film is possibly higher than that of the spatially

ordered mesh Au film. So, the observed redshift and asymmetric broadening of spectral lines for disordered arrays are much more pronounced than those of ordered arrays. The primary reason for this phenomenon may be related to the electrical conductivity of noble metals. The conductivity of Au as a catalyst is stronger than that of Ag. The enhancement of metal conductivity enables electrons to be transmitted as fast as possible to the interface between the metal film and the solution. Meanwhile, protons do not have enough time to diffuse to the interface between the metal film and the silicon wafer, thus forming a concentration gradient, which means that the metal particles are in a larger self-built electric field, accelerating the etching rate [31,32]. The higher transfer rate of carriers means that the process of carrier relaxation, recombination and deep-level defect state binding in the system can be effectively avoided. Previous studies reported that the etching rate of a silicon wafer is very sensitive to local strain. Assuming that nanowires continue to form after the initial etching, exposed surfaces with tensile strain need to be stabilized by lattice shrinkage. Then, the residual strain effect is very significant in extreme cases, which possibly leads to nonlinear elastic deformation, superelasticity and even lattice phase transitions, resulting in changes in the measured Raman spectral curve.
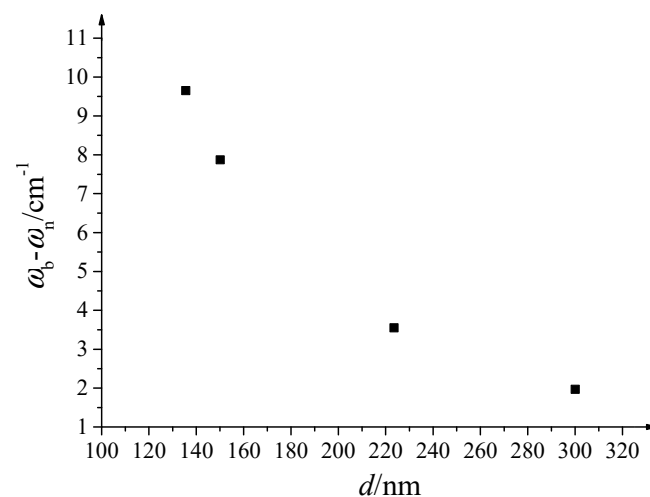

Figure 8. The relationship curve between $\omega_b - \omega_n$ and d.

As depicted in Figure 5, the redshifts of the scattering peaks of the two morphologically different arrays after annealing are smaller than those before annealing, with stronger symmetry and weaker peak broadening. The silicon atoms deviating from the lattice position receive enough energy to snap back to the vacancies at lattice node positions. The small defect clusters and lattice stress are gradually restored as heat is applied. The roughness of the side wall of the silicon wires could cause phonon scattering. The crystal defect causes the propagation of phonon waves in materials to be attenuated, leading to the relaxation of the momentum conservation rule. That is, some $k \neq 0$ phonons are also excited. This manifests as the asymmetry and broadening of the Raman spectral shape, thus causing the change in the phonon spectrum.

$$I(\omega) \propto \int_0^1 \exp\left(-\frac{k^2 L^2}{4}\right) \frac{dk^2}{[\omega - \omega(k)]^2 + [\Gamma_0/2]} \tag{2}$$

where ω is the phonon frequency; k is the wave vector of the phonon; L is the correlation length, associated with the density of defects in crystals; and Γ_0 is the half-peak width of the Raman spectra for the complete crystal. Considering the phonon dispersion relation near the center of the Brillouin zone,

$$\omega(k) = A + B\cos(\pi k) \tag{3}$$

The relationship between the redshift of the Raman peak, the correlation length *L* and the half-peak width Γ_0 can be calculated by using Formulas (2) and (3). Beyond that, another possibility is that SiNWs lacking a passivation layer possess extremely high effective surface recombination velocity. It is speculated that some areas of ordered SiNWs could be effectively passivated by the residual AAO, which exhibited a promising effective carrier lifetime upon post-deposition annealing. Van Hoang Nguyen et al. [33] demonstrated that the effective carrier lifetime of SiNWs drastically increased upon post-deposition annealing under thermal treatment at about 650 °C. This is possibly due to the carriers easily diffusing because of a reduction in defects at the bottom of the SiNWs. S. Ben Dkhil et al. [34] concluded that thermal annealing gave rise to a reduction in the charge separation efficiency and thus in their transfer at the interface between the substrate and silicon nanowires.

The finite linewidth of SiNWs gives rise to confined modes, causing asymmetry and an increase in the Raman scattering intensity compared with the red line in the low-frequency region of the longitudinal optical (LO) or transverse optical (TO) phonon peaks [35]. As the crystallite is reduced to the nanoscale, the phonons with a wave vector participate in first-order Raman scattering. The wave-vector balance may be broken, resulting in the appearance of surface and interface vibration modes. Phonon scattering that is not limited to the center of the Brillouin zone of the Raman spectra can be taken into account [27]. In Figure 5, the full width at half maximum (FWHM) on the pre-maximum side is increased due to the quantum confinement effect, resulting in asymmetric broadening toward the lower-energy side of the main peak [36]. It is clear that the FWHM of the main peak after annealing is much lower than that before annealing, as illustrated in Table 1, indicating that annealing improves the compactness of the film, which is also consistent with the microstructure observed by high-resolution SEM in Figure 4. In addition, the existence of the Fano interaction caused by heavily doped p-type silicon used in the experiment could induce an increased half-width in the post-maximum side [18]. The amorphous silicon oxide layer formed on the silicon nanowire surface after etching and the existence of structural defects in SiNWs can also strongly influence the change in the Raman scattering peak [37].

Table 1. TO peak information of four samples after fitting.

	Peak Intensity /Counts	Full Width at Half Maximum/cm^{-1}	Peak Area /cm^{-1} Counts·
Disordered SiNWs before annealing	33,838.4	19.91	717,321
Disordered SiNWs after annealing	29,273.6	8.632	268,981
Ordered SiNWs before annealing	70,816.7	15.41	939,731
Ordered SiNWs after annealing	67,633.2	10.91	808,686

In addition to the above factors, it is necessary to analyze the effects of other various mechanisms on the observed symmetry-forbidden mode of the Raman curve for a further understanding of the crystal structures of the samples. It is widely known that laser irradiation (incident light power exceeding several milliwatts) sparks the frequency redshift of scattering peaks for silicon wires. It is difficult to release the heating energy accumulated inside the silicon wires because of the small contact area with the substrate. Scientists are concerned about the thermal conductivity of silicon nanowire arrays. Al Hochbaum et al. noted that [38] SiNWs with diameters of about several tens of nanometers exhibit a 100-fold reduction in thermal conductivity compared with doped bulk silicon, even if both have the same Seebeck coefficient and electrical resistivity values. However, the dependence of the observed redshift of the main Raman mode on thermal conductivity is not as clear. G.S. Doerk et al. [39] demonstrated that no changes in lattice anharmonicity occur in relation to the silicon nanowire size; thus, the observed effect is probably due to the poor control of the sample temperature during spectroscopic measurements.

The asymmetry of the Raman peak lineshape is possibly also caused by Fano interaction in the material. The Auger effect indicates that electrons in the inner layer of the atom are stimulated by ionization to form vacancies. The electrons at higher energy levels that transition to these vacancies release energy, and other electrons in the outer layer of the atom absorb this energy and are stimulated. Stimulated electrons follow autoionization via the Auger effect and the direct ionization of inner electrons, as shown in Figure 9.
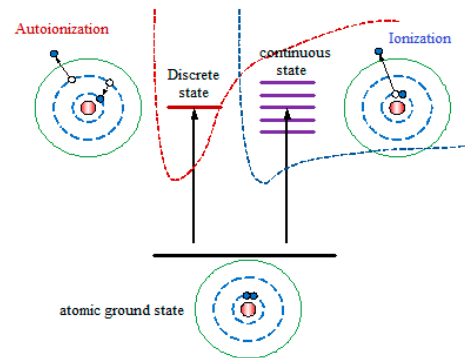

Figure 9. The two modes of the photoionization of atoms.

The transition from the atomic ground state to the discrete state and from the atomic ground state to the continuum state are the two modes of atomic photoionization. The symmetrically distributed discrete state and the wide-spectrum continuous state are coupled to different paths, giving rise to asymmetric linear resonance through quantum interference. This observed asymmetric Breit–Wigner–Fano (BWF) lineshape of Raman spectra satisfies the following formula [40]:

$$I_{\mathrm{BWF}}(\omega_S) = I_0 \left[\frac{1}{q_{\mathrm{BWF}}^2} + \frac{1 - 1/q_{\mathrm{BWF}}^2}{1 + s^2} + \frac{2s/q_{\mathrm{BWF}}}{1 + s^2} \right] \tag{4}$$

where $s = (\omega_{\mathrm{s}} - \omega_{\mathrm{G}})/\Gamma$, ω_{s} is the Raman shift, ω_{G} is the spectral peak position and Γ is the spectral width. $1/q_{\mathrm{BWF}}$ is the asymmetric factor; I_0 is the maximum intensity of the spectra. The above formula contains three terms: the constant continuum spectrum, the discrete Lorentzian spectrum and the interference effect between the two spectra. The asymmetric factor affecting the spectrum for SiNWs accounts for the various transition probabilities of internal electrons. First of all, the asymmetric lineshape could have occurred via the transition of free electrons in the conduction band, releasing low energy, owing to the energy reduction at the bottom of the conduction band caused by long-wave optical phonons. The overlap between the electronic continuum and discrete states causes interference effects, and Fano interference arises [41]. The possible explanation is that the interference between the electronic Raman spectra and the phonon spectra leads to a great change in the constructive/destructive interference near the phonon spectra, which brings about additional asymmetry in the phonon lineshape fitting to the BWF lineshape [40].

5. Conclusions

The above discussion indicates that changes in measured Raman spectral curves originate from various mechanisms, the most important of which are the quantum effect caused by etching bulk silicon at the nanoscale, the formation of structural defects in the constituting areas and stress produced in the etching process. Our present results demonstrate that some of the Raman scattering peak's deviation from symmetry, redshift and broadening are likely related to the type and morphology of the noble metal catalyst used in the preparation of SiNWs. It is further deduced from the experiment that the annealing process can improve internal lattice defects and enhance the effective carrier lifetime. This point is confirmed by the finding that the observed Raman scattering peak after annealing weakens the redshift and asymmetric broadening of the spectrum, which is more similar to

the Raman spectrum of monocrystalline silicon. Therefore, the deviation of SiNWs from the monocrystalline silicon scattering peak at 520.05 cm^{-1} when changing the diameter of the nanowire columns through thermal expansion was calculated to further analyze the effect of thermal annealing on Raman characteristics. We came to the conclusion that the redshift characteristics arise as the diameter of the nanowire columns increases. For each 150 nm increase in diameter, the deviation decreases by approximately 5.9 cm^{-1}. SiNWs offer a significant cost advantage over traditional crystalline silicon technologies, such as the silane technique and monomer copolymerization method. At present, novel fabrication methods for simple, cost-effective, large-area growth with surface-enhanced Raman scattering are thus of great importance for various practical applications. Nevertheless, there is still a manufacturability problem related to the deposition of noble metals on the surface of silicon wafers and the chemical etching process, resulting in more lattice defects than obtained on textured surfaces with other methods, such as laser ablation. The way to avoid these problems is the focus of the next stage. The present results provide insight for exploring the potential applications of SiNWs in photovoltaic devices and photoelectric sensors, which have led to the search for means of improving the spectral responsivity of micro-/nanostructured Si-based materials.

Author Contributions: Conceptualization, S.W.; Methodology, S.W.; Validation, S.W.; Formal analysis, S.W.; Investigation, S.W.; Resources, Y.Z.; Data curation, Y.Z.; Writing—original draft, S.W.; Writing—review & editing, S.W. All authors have read and agreed to the published version of the manuscript.

Institutional Review Board Statement: Not applicable.

Informed Consent Statement: Not applicable.

Data Availability Statement: Not applicable.

Conflicts of Interest: The authors declare no conflict of interest.

References

1. Sahoo, M.; Kale, P. Micro-raman study of growth parameter restraint for silicon nanowire synthesis using MACE. *Superlattices Microstruct.* **2019**, *135*, 106289. [CrossRef]
2. Theresa, B.; Wendisch, F.J.; Farhandi, A.; Bourret, G.R. Recent advances in structuring and patterning silicon nanowire arrays for engineering light absorption in three dimensions. *ACS Appl. Energy Mater.* **2022**, *5*, 5307–5317.
3. Sahoo, M.; Kale, P. Integration of silicon nanowires in solar cell structure for efficiency enhancementa review. *J. Mater.* **2019**, *5*, 34–48.
4. Georgobiani, V.; Gonchar, K.; Zvereva, E.; Osminkina, L. Porous silicon nanowire arrays for reversible optical gas sensing. *Phys. Status Solidi* **2018**, *215*, 1700565. [CrossRef]
5. Lin, H.; Jiang, A.; Xing, S.; Li, L.; Cheng, W.; Li, J.; Mia, W.; Zhou, X.; Tian, L. Advances in self-powered ultraviolet photodetectors based on P-N heterojunction low-dimensional nanostructures. *Nanomaterials* **2022**, *12*, 910. [CrossRef]
6. Miao, F.; Miao, R.; Wu, W.; Cong, W.; Zang, Y.; Tao, B. A stable hybrid anode of graphene/silicon nanowires array for high performance lithium-ion battery. *Mater. Lett.* **2018**, *228*, 262–265. [CrossRef]
7. Lu, Z.; Zhou, H.; Wang, Y.; Liu, Y.; Le, T. A controllable fabrication improved silicon nanowire array sensor on (111) SOI for accurate bio-analysis application. *Nano Res.* **2022**, *15*, 7468–7475. [CrossRef]
8. Farid, G.; Yang, Y.; Mateen, A.; Huo, C.; Wang, H.; Peng, K.-Q. Rapid formation of uniform cracks in metal-assisted etched silicon nanowire array membranes: Implications for transfer of nanowires and flexible devices. *ACS Appl. Nano Mater.* **2022**, *5*, 2779–2786. [CrossRef]
9. Schweidler, S.; Dreyer, S.L.; Breitung, B.; Brezesinski, T. Acoustic emission monitoring of high-entropy oxyfluoride rock-salt cathodes during battery operation. *Coatings* **2022**, *12*, 402. [CrossRef]
10. Dong, Y.; Mai, L.; Jin, S.; Girard, S.N.; Li, L.; Stolt, M.J.; Slade, T. Low temperature molten salt production of silicon nanowires by electrochemical reduction of $CaSiO_3$. *Angew. Chem. Int. Ed.* **2017**, *56*, 14453–14457. [CrossRef]

11. Okazoe, T.; Shirakawa, D.; Murata, K. Application of liquid-phase direct fluorination: Novel synthetic methods for a polyfluorinated coating material and a monomer of a perfluorinated polymer electrolyte membrane. *Appl. Sci.* **2012**, *2*, 327–341. [CrossRef]
12. Sen, G.; Sanghyun, H.; Soohyung, P.; Jung, H.Y.; Liang, W.; Lee, Y.; Ahn, C.W.; Byun, J.Y.; Sep, J.; Hahm, M.G.; et al. Catalyst-free synthesis of sub-5 nm silicon nanowire arrays with massive lattice contraction and wide bandgap. *Nat. Commun.* **2022**, *13*, 3467.
13. Sun, L.; Fan, Y.; Wang, X.; Susantyoko, R.A.; Zhang, Q. Large scale low cost fabrication of diameter controllable silicon nanowire arrays. *Nanotechnology* **2014**, *25*, 255302. [CrossRef] [PubMed]
14. Mohamedyaseen, A.; Kumar, P.S.; Kavitha, K.R.; Vignesh, N.A. Anisotropy enhancing vertically aligned silicon-germanium nanowire. *Silicon* **2022**, *14*, 12177–12184. [CrossRef]
15. Huang, Z.; Geyer, N.; Werner, P.; de Boor, J.; Gösele, U. Metal-assisted chemical etching of silicon: A review. *Adv. Mater.* **2011**, *23*, 285–308. [CrossRef]
16. Mao, J.; Li, J.; Pei, J.; Liu, Y.; Wang, D.; Li, Y. Structure regulation of noble-metal-based nanomaterials at an atomic level. *Nano Today* **2019**, *26*, 164–175. [CrossRef]
17. Wang, S.; Liu, H.; Han, J. Comprehensive study of Au nano-mesh as a catalyst in the fabrication of silicon nanowires arrays by metal-assisted chemical etching. *Coatings* **2019**, *9*, 149. [CrossRef]
18. Saxena, S.K.; Borah, R.; Kumar, V.; Rai, H.M.; Late, R.; Sathe, V.M.; Kumar, A.; Sagdeo, P.R.; Kumar, R. Raman spectroscopy for study of interplay between phonon confinement and Fano effect in silicon nanowires. *J. Raman Spectrosc.* **2016**, *47*, 283–288. [CrossRef]
19. Wang, S.; Huang, S.; Zhao, J. Effect of surface morphology changes on optical properties of silicon nanowire arrays. *Sensors* **2022**, *22*, 2454. [CrossRef]
20. Yevgeniya, L.; Mircea, T.; Sina, R.; Dominic, T.; Jan, K.; Tobias, W.; Uwe, H.; Jan-Dirk, K.; Robby, P. On the recombination behavior of p(+)-type polysilicon on oxide junctions deposited by different methods on textured and planar surfaces. *Phys. Status Solidi (A) Appl. Mater. Sci.* **2017**, *214*, 1700058.
21. Bian, C.; Zhang, B.; Zhang, Z.; Chen, H.; Zhang, D.; Wang, S.; Ye, J.; He, L.; Jie, J.; Zhang, X. Wafer-scale fabrication of silicon nanocones via controlling catalyst evolution in all-wet metal-assisted chemical etching. *ACS Omega* **2022**, *7*, 2234–2243. [CrossRef]
22. Wang, S.; Han, J.; Yin, S. The effect of silver-plating time on silicon nanowires arrays fabricated by wet chemical etching method. *Opt. Photonics J.* **2019**, *9*, 1–10. [CrossRef]
23. Wang, S.; Han, J.; Song, D.; Wang, X. Effect of NaOH solution concentration on the quality of controllable silicon nanowires array fabrication. *Mater. Res. Express* **2019**, *6*, 1250.e9. [CrossRef]
24. Carey, J.; Crouch, C.; Shen, M.; Mazur, E. Visible and near-infrared responsivity of femtosecond-laser microstructured silicon photodiodes. *Opt. Lett.* **2005**, *30*, 1773–1775. [CrossRef] [PubMed]
25. Cao, L.P.; Chen, Z.D.; Zhang, C.L. Effect of thermal annealing on sub-band-gap absorptance of microstructured silicon in air. *Front. Phys.* **2015**, *10*, 1–7. [CrossRef]
26. Zhao, T.; Peng, Y.; Miao, Q.; Li, B.; Liang, K.; Yang, R.; Han, D. One-dimensional single-photon position-sensitive silicon photomultiplier and its application in Raman spectroscopy. *Opt. Express* **2017**, *25*, 22820–22828. [CrossRef]
27. Wang, R.; Zhou, G.; Liu, Y.; Pan, S.; Zhang, H.; Yu, D.-P.; Zhang, Z. Raman spectral study of silicon nanowires: High-order scattering and phonon confinement effects. *Phys. Rev. B* **2000**, *61*, 16827. [CrossRef]
28. Yuan, X.; Mayanovic, R.A. An empirical study on raman peak fitting and its application to raman quantitative research. *Appl. Spectrosc. Soc. Appl. Spectrosc.* **2017**, *71*, 2325–2338. [CrossRef]
29. Huang, Y.; Liu, X.; Chao, W.Z.; Xu, C.G.; Chun, W.L.; Dong, Y.S. Study of nano-crystalline silicon films. *Sci. China Ser. A* **1993**, *36*, 248–256.
30. Cheng, G. Nano-structural and thin film materials studies by raman and brillouin scattering. *J. Light Scatt.* **2010**, *22*, 196–206.
31. Peng, K.; Gao, S.; Zhu, J. Synthesis of large-area silicon nanowire arrays via self-assembling nanoelectrochemistry. *Adv. Mater.* **2002**, *14*, 1164–1167. [CrossRef]
32. Peng, K.Q.; Hu, J.J.; Yan, Y.J.; Wu, Y.; Fang, H.; Xu, Y.; Lee, S.T.; Zhu, J. Fabrication of single-crystalline silicon nanowires by scratching a silicon surface with catalytic metal particles. *Adv. Funct. Mater.* **2006**, *16*, 387–394. [CrossRef]
33. Nguyen, V.H.; Sichanugrist, P.; Kato, S.; Usami, N. Impact of anodic aluminum oxide fabrication and post-deposition anneal on the effective carrier lifetime of vertical silicon nanowires. *Sol. Energy Mater. Sol. Cells* **2017**, *166*, 39–44. [CrossRef]
34. Dkhil, S.B.; Davenas, J.; Bourguiga, R.; Cornu, D. Effect of thermal treatments on the properties of PVK/silicon nanowires films for hybrid solar cells. *Synth. Met.* **2011**, *161*, 1928–1933. [CrossRef]
35. Cantarero, A. Review on Raman scattering in semiconductor nanowires: I. theory. *J. Nanophotonics* **2013**, *7*, 071598. [CrossRef]
36. Priyanka, Y.; Deepika, P.; Suryakant, M.; Shailendram, K.S.; Swarup, R.; Vivek, K.; Pankajm, R.S.; Rajesh, K. Spectral anomaly in raman scattering from p-type silicon nanowires. *J. Phys. Chem. C* **2017**, *121*, 5372–5378.
37. Piscanec, S.; Cantoro, M.; Ferrari, A.C.; Zapien, J.A.; Lifshitz, Y.; Lee, S.T.; Hofmann, S.; Robertson, J. Raman spectroscopy of silicon nanowires. *Phys. Rev. B* **2003**, *68*, 241312. [CrossRef]
38. Hochbaum, A.; Chen, R.; Delgado, R.; Liang, W.; Garnett, E.; Najarian, M.; Majumdar, A.; Yang, P. Enhanced thermoelectric performance of rough silicon nanowires. *Nature* **2008**, *451*, 163–167. [CrossRef]
39. Doerk, G.S.; Carraro, C.; Maboudian, R. Temperature dependence of Raman spectra for individual silicon nanowires. *Phys. Rev. B* **2009**, *80*, 073306. [CrossRef]

40. Hasdeo, E.H.; Nugraha, A.R.T.; Dresselhaus, M.S.; Saito, R. Breit-Wigner-Fano line shapes in Raman spectra of graphene. *Phys. Rev. B* **2014**, *90*, 245140. [CrossRef]
41. Burke, B.G.; Chan, J.; Williams, K.A.; Wu, Z.; Puretzky, A.A.; Geohegan, D.B. Raman study of Fano interference in p-type doped silicon. *J. Raman Spectrosc.* **2010**, *41*, 1469–1474. [CrossRef]